Article:
Trapalis, A., Heffernan, J., Farrer, I. et al. (2016) Structural, electrical, and optical characterization of as grown and oxidized zinc nitride thin films. Journal of Applied Physics, 120. 205102. ISSN: 1089-7550

https://doi.org/10.1063/1.4968545

Structural, electrical and optical characterization of as grown and oxidized zinc nitride thin films

A. Trapalis[1], J. Heffernan[1,a)], I. Farrer[1], J. Sharman[2], A. Kean[2,3]

[1]*Department of Electronic and Electrical Engineering, University of Sheffield, Mappin Street, Sheffield S1 3JD, United Kingdom.*

[2]*Johnson Matthey, Blount's Court, Sonning Common, Reading RG4 9NH, United Kingdom.*

[3]*NikaWorks Ltd, Watlington, Oxfordshire OX49 5JT, United Kingdom.*

Zinc Nitride (Zn_3N_2) films were grown by DC sputtering of a Zn target in N_2 plasma under a variety of different growth conditions which resulted in the deposition of films with variable composition. The as deposited films exhibited a polycrystalline Zn_3N_2 structure which was converted to a ZnO-based structure after several weeks of ambient exposure. Zn_3N_2 films that were N-poor exhibited electrical properties indicative of a natively doped semiconductor and reached a minimum carrier concentration in the order of 10^{18} cm^{-3} at compositions which approached the stoichiometric ratio of Zn_3N_2. A maximum carrier mobility of 33 cm^2 V^{-1} s^{-1} was obtained in N-rich films due to an improved microstructure. The Zn_3N_2 films had an optical band gap of 1.31-1.48 eV and a refractive index of 2.3-2.7. Despite a wide range of Zn_3N_2 samples examined, little variation of its optical properties was observed, which suggests they are closely related to the band structure of this material. In contrast to the as grown films, the oxidized film had a band gap of 3.44 eV and the refractive index was 1.6-1.8, similar to ZnO and $Zn(OH)_2$.

I. INTRODUCTION

Zinc Nitride (Zn_3N_2) is a semiconductor of the II-V semiconductor group which has recently gained attention for its potential applications in a number of large industrial markets including solar cells, thin film transistors and other optoelectronic devices[1-5]. The potential of Zn_3N_2 for these applications stems primarily from the electrical properties of polycrystalline Zn_3N_2 films which commonly exhibit a high charge carrier mobility[6-11]. In addition, the narrow band gap of 1.2-1.4 eV and high absorption coefficient that are often associated with Zn_3N_2 make it a potential candidate for the fabrication of thin films solar cells[12]. Furthermore, the relative abundance of Zn and N as well as low-cost fabrication techniques such as magnetron sputtering also make Zn_3N_2 a good candidate for the fabrication of low-cost devices. Despite this potential, Zn_3N_2 is not as well researched as III-V semiconductors such as AlN, GaN and InN and there are conflicting reports in the literature on the basic properties of the semiconductor.

In recent published literature, Zn_3N_2 is most often synthesized in the form of powder or films by nitridation of Zn powder[13-16] and DC/RF sputtering[6,7,17-22]. However, a variety of synthesis methods and techniques have been reported including a chemical reaction of diethyl zinc with ammonia[23], electrolysis[24], atomic layer deposition[25], pulsed laser ablation[26,27], chemical vapor deposition[28-30] and molecular beam epitaxy[11,31]. Due to the large lattice constant of its crystal structure, suitable substrates for the epitaxial growth of Zn_3N_2 have not been established. As a result, Zn_3N_2 films grown on different glass, sapphire, quartz and silicon substrates commonly exhibit a polycrystalline structure. However, Oshima and Fujita have reported the growth of (111)-oriented Zn_3N_2 on a-plane sapphire by molecular beam epitaxy and suggested that a-plane sapphire is a suitable substrate for heteroepitaxial growth of high-quality Zn_3N_2[31].

In terms of electrical properties, Zn_3N_2 films are usually n-type and exhibit charge carrier concentrations in the order of 10^{18} – 10^{21} cm^{-3}. The high carrier concentration and n-type conductivity have been associated with N vacancies and other native defects in the lattice which introduce free carriers[32]. Due to the high carrier concentration levels, Zn_3N_2 films have been reported to behave as degenerate semiconductors[33]. Despite that, a carrier mobility in the order of 10^2 cm^2 V^{-1} s^{-1} is commonly reported for Zn_3N_2 films, which is high when compared with other polycrystalline semiconductors. This suggests that optimization in material quality may lead to further improvement of its electrical properties.

One of the key properties of any semiconductor is its optical band gap, and in the case of Zinc Nitride, this remains a subject of debate in the literature. Synthesized Zn_3N_2 with band gap energies in the range of 0.9-3.2 eV have been reported[1,6,33] and there is a similar spread in the reported values of the refractive index of Zn_3N_2 materials, with values of 1.7-1.9 when it is reported as a wide band gap semiconductor[27,34] and 2.2-2.8 when reported as a narrow band gap semiconductor[18,35]. These large discrepancies have caused confusion with regards to potential applications for this material. While the differences between different reports are usually attributed to the different fabrication methods and material quality in each study, two opposing arguments have been made to explain these observations. On one hand, it has been suggested that the narrow observed band gap is related to N interstitial defects which lower the optical band gap of Zn_3N_2 by introducing half-filled states in the electronic structure[33]. On the other hand, observations of a wide band gap are sometimes attributed to the formation of an oxide phase or the unintentional incorporation of oxygen into the lattice[10], which is believed lead to an overestimation of the optical band gap of the pure Zn_3N_2 phase.

An important aspect of Zn_3N_2 that may be the source of the variable properties reported in the literature is its poor ambient stability as a result of its reactions with O_2 and H_2O in air[24]. The reactions are not self-limiting and can lead to complete conversion of Zn_3N_2 after prolonged exposure[36], which makes the ambient stability a factor that has to be accounted for when considering potential applications. However, Núñez, Pau et al. have reported that an intentionally grown 20 nm thick ZnO capping layer can successfully prevent this oxidation process and opens an avenue for optimizing the material for applications.

In the present work, Zn_3N_2 films were prepared by DC magnetron sputtering in a range of different N_2 environments and substrate temperatures with the intention of achieving a wide range of different materials. The composition, crystal structure and the optical and electrical properties of the films were characterized. In addition, the crystal structure and optical properties of a fully oxidized sample were also investigated. Emphasis was placed on interpreting the differences between the samples grown at different conditions, as well as the differences between the as grown and oxidized material, in order to further our understanding of the fundamental properties of Zn_3N_2.

II. EXPERIMENTAL

A. Film growth

The Zn_3N_2 thin films in this study were grown on borosilicate glass slides by reactive sputtering of a Zn target in N_2 plasma in a Denton Vacuum Explorer sputterer. A constant flow of only N_2 gas was used to achieve plasma in the chamber which also acted as the source of active N species for the reaction with sputtered Zn atoms. The sputtering process was conducted with a DC power source with the current set to 200 mA for the duration of the sputtering process. Prior to

deposition, the Zn target was sputtered in Ar plasma for 15 mins with the shutter closed in order to remove any surface contaminants from the target. The base pressure in the chamber was 6×10^{-7} Torr and the operating pressure was in the order of 10^{-3} Torr. Films were grown at room temperature at N_2 flow rates of 15, 30 and 45 SCCM. At the highest N_2 flow rate, films were also grown at substrate temperatures of 50, 100 and 150 °C. The sputtering process resulted in the deposition of opaque dark films which became fully transparent after several weeks of exposure to ambient air.

TABLE I: Growth conditions and thickness of the Zn_3N_2 samples examined in this study.

Nominal Name	**N_2 gas flow (SCCM)**	**Substrate Temperature (°C)**	**Growth Duration (min)**	**Thickness (nm)**
ZnN-1	15	20	15	461
ZnN-2	30	20	27	481
ZnN-3	45	20	60	735
ZnN-4	45	50	70	886
ZnN-5	45	100	70	853
ZnN-6	45	150	70	365
ZnN-3A	45	20	60	1132

B. Characterization

A combination of physical, optical and electrical characterization techniques was applied to all films. Scanning Electron Microscopy (SEM) images of the surface morphology of the films were recorded on a Raith Field Emission Scanning Electron Microscope (FESEM) with an

accelerating voltage of 10 kV. The thickness of each sample was evaluated by cross-sectional SEM images which were recorded with an accelerating voltage of 2 kV. Film composition was evaluated by the quantification of Energy Dispersive X-ray Spectroscopy (EDS) measurements acquired with a Bruker Quantax EDS system installed on the Raith FESEM. The quantification of the EDS spectra was carried out using a standardless P/B-ZAF analysis technique provided by the Bruker ESPRIT software. Grazing incidence X-ray Diffraction (GI-XRD) was conducted on a Bruker D8 DISCOVER diffractometer and the measured 2θ range of 30 to 80° was scanned at a rate of 0.05°/sec. The electrical properties of the films were evaluated by Hall Effect measurements acquired on an Ecopia HMS-5000 Hall Effect system.

For optical characterization, transmittance and reflectance measurements in the spectral range of 300-1700 nm were recorded on a J.A. Woollam RC2 ellipsometer. The optical transmittance and reflectance measurements were used to calculate the absorption coefficient of each film with the following equation[37]:

$$a = \frac{1}{\mathrm{d}} \ln \frac{\frac{(1-R)^2}{T} + \sqrt{\frac{(1-R)^4}{T^2} + 4R}}{2} \quad (1)$$

where α, d, R and T are the absorption coefficient, thickness, reflectance and transmittance of the film respectively. We also calculated the spectrally dependent refractive indices of each film from the constructive and destructive interference points in the reflectance spectrum, using the following equation:

$$2nd\ cos\beta = \left(m - \frac{1}{2}\right)\lambda_r \quad (2)$$

where n and d are the refractive index and thickness of the film respectively, β is the angle of the beam inside the film calculated by Snell's law, m is the order of the reflection and λ_r is the wavelength of the maximum reflection. The order of the measured reflections was determined by growing films thin enough to observe the first order reflection.

Due to the tendency of Zn_3N_2 to oxidize at ambient environments, all characterization was done immediately after deposition and with minimal exposure to ambient air. The stability of the samples was monitored by repeating optical measurements. Cross-sectional SEM also showed that all aged samples exhibited an expansion of 50-60% in thickness. The sample grown at room temperature and a N_2 flow rate of 45 SCCM was chosen as a representative oxidized sample. Alongside other results, Section III discusses XRD and optical measurements of this sample after 54 days of exposure to air, which were enough to allow its complete conversion to a transparent medium. Throughout the manuscript, the as-grown sample is labelled as ZnN-3, while its aged counterpart is labelled as ZnN-3A. A detailed description of the samples examined in this study is given in **Table I**.

III. RESULTS AND DISCUSSION

A. Morphological, compositional and structural characterization

The morphology and microstructure of the grown films were initially investigated by SEM. The images in **Fig. 1** show the surface of samples ZnN-1 to ZnN-6 at 160,000x magnification. Sample ZnN-1 consisted of randomly oriented flakes, but a clear grain structure emerged in samples ZnN-2 to ZnN-6 as the N_2 flow rate increased. The grains were approximately rhombic in shape with lateral dimensions of around 100 nm. As the substrate temperature increased in samples ZnN-5 and ZnN-6, the grain boundaries started to coalesce and became less apparent. The surface of sample ZnN-6 in particular appeared to be very smooth and more uniform than that of the other samples.

In order to relate the composition of the films to their structure and their electrical and optical properties, we used a quantitative EDS analysis. The following characteristic X-rays were

identified in all samples: C: Kα at 0.277 keV, N: Kα at 0.392 keV, O: Kα at 0.525 keV and several Zn: L lines (Ll, Le, Lα, Lβ) in the region of 0.882-1.108 eV[38,39]. The compositional data obtained from analysis of the EDS spectra are listed in **Table II**. We note that a varying amount of carbon and oxygen (3-6 at. % and 5-13 at. % respectively) was detected in all samples. However, decreasing the penetration depth of the electron beam resulted in an increase of their concentration, which suggests a significant portion of the carbon and oxygen can be attributed to the surface contamination and oxidation of the samples respectively. Therefore, for the purpose of this paper, the calculated Zn:N atomic ratio was considered indicative of the composition in the bulk of the films.

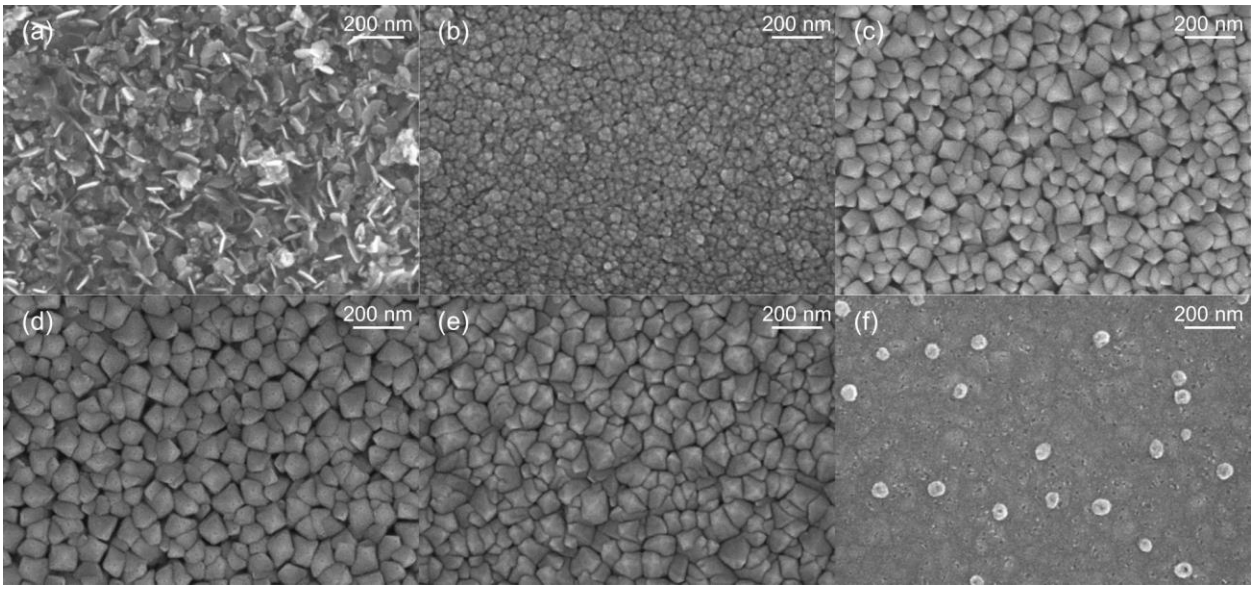

FIG. 1: SEM images of samples: (a) ZnN-1, (b) ZnN-2, (c) ZnN-3, (d) ZnN-4, (e) ZnN-5 and (f) ZnN-6 at 160,000x magnification.

The Zn:N atomic ratio for samples grown at different conditions is shown in **Fig. 2**. It can be noted in **Fig. 2a** that the film composition approached stoichiometry at higher N_2 flow rates. Specifically, as the N_2 flow rate increased the average Zn:N ratio decreased from 1.92 to 1.55. At higher substrate temperatures, the average Zn:N ratio decreased further to 1.52, 1.41 and 1.27, as

shown in **Fig. 2b**. The improvement of the stoichiometry at higher N_2 flows is explained by the increase in pressure which made reaction between Zn atoms and N ions more likely. At higher substrate temperatures, the decrease of Zn content can be explained by a thermally activated reemission of excess Zn particles during growth.

The experimental errors between multiple measurements made at different positions on each ~1 cm^2 sample were insignificant and are not displayed. The error bars displayed in **Fig. 2** represent the systematic errors estimated by the analysis software, which are based on internal standards and depend on the elements that are measured. While these errors are significant, resulting to approximately 16% relative error in the calculated Zn:N ratio, they are typical of standardless EDS analysis[40]. However, there is enough supporting evidence from analysis of XRD, Hall Effect and optical measurements, discussed in the following sections, to suggest that the observed trend is real.

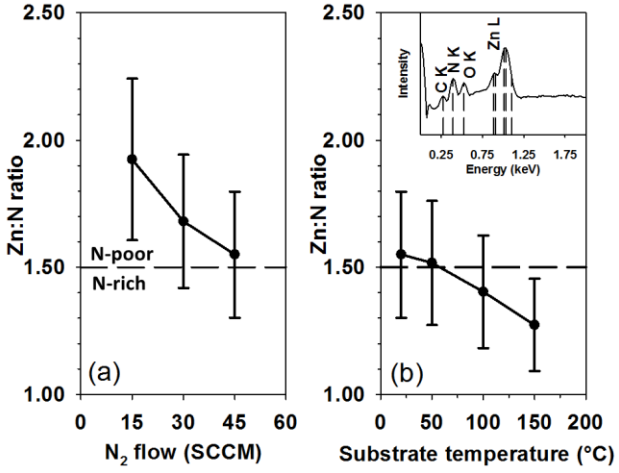

FIG. 2: Zn:N atomic ratio of grown samples as a function of (a) N_2 flow and (b) substrate temperature. The dashed line marks the stoichiometric Zn:N ratio of Zn_3N_2. Inset: The EDS spectrum of ZnN-3.

Having confirmed the presence of Zn and N in the grown samples with EDS analysis, further structural information was obtained by XRD measurements. The XRD patterns of the

samples grown at different conditions are shown in **Fig. 3**. Several diffraction peaks of the cubic anti-bixbyite Zn_3N_2 crystal structure[15,23,41] were identified in samples ZnN-1 to ZnN-6. The relatively broad and weak features observed in samples ZnN-1, ZnN-2 and ZnN-6 suggest a defective polycrystalline structure. In sample ZnN-1 specifically, there is an overlap between some of the peaks of the Zn_3N_2 and Zn crystal structures, making interpretation of this diffraction pattern more difficult. These are marked by the asterisks in **Fig. 3** and correspond to the (100), (101), (102) and $(2\bar{1}0)$ diffraction peaks of the Zn crystal structure which are expected to be at 39.09, 43.33, 54.46 and 70.82° respectively[42]. The disappearance of some of these features in the XRD pattern of ZnN-2 suggests they are related to a Zn phase which is evident only in the sample grown at the most N-poor conditions. In contrast, the narrower features observed in samples ZnN-3, ZnN-4 and ZnN-5 show that there was an improvement in the crystal structure of the films grown at the highest N_2 flow of 45 SCCM and substrate temperatures of 20-100 °C. Furthermore, the (400) peak became the dominant feature of the diffraction patterns of the samples grown under these conditions, which shows that the films tend to crystallize with a (100) orientation, as has been reported previously[17]. Based on the positions of the (400) and (440) diffraction peaks, the lattice constant of the Zn_3N_2 crystal structure was calculated at 9.76 Å, which is in good agreement with previous reports[15,41,43]. Finally, the XRD pattern of the sample ZnN-3A revealed that the Zn_3N_2 films were converted to a polycrystalline ZnO-based phase after prolonged exposure to ambient air[44]. The large full-width half-maximum of these diffraction peaks shows there is a large number of structural defects in the oxidized material. However, the difference between the diffraction patterns of this sample and the as deposited samples is clear evidence that they are distinctly different materials.

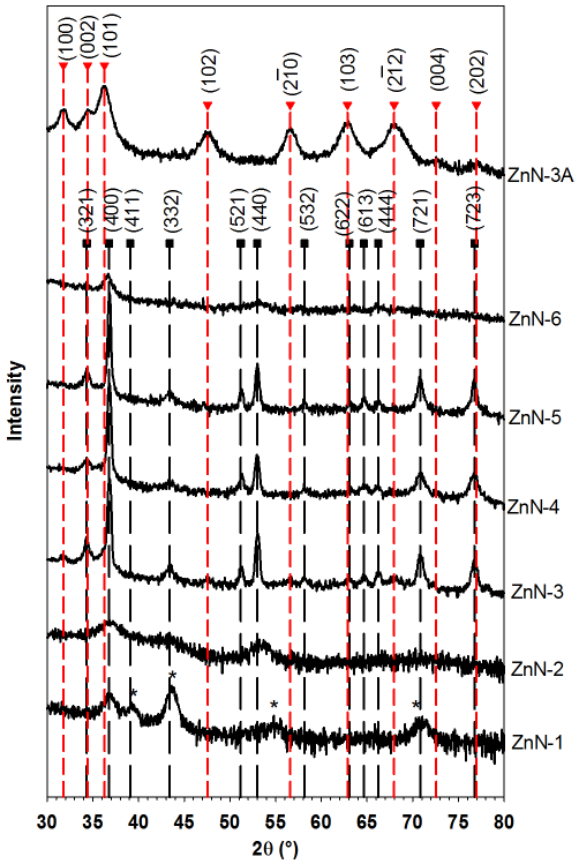

FIG. 3: XRD patterns of Zn_3N_2 samples grown at different conditions. Rectangles and triangles indicate diffraction peaks attributed to crystal planes of the Zn_3N_2 and ZnO crystal structures respectively. The asterisks in the XRD pattern of ZnN-1 indicate some features which are potentially caused by a Zn crystal phase.

The results of the XRD measurements seem to be in agreement with the morphological and compositional analysis made by SEM/EDS. As seen in **Fig. 1**, a more defined grain structure was formed in the better crystallized ZnN-3, ZnN-4 and ZnN-5 samples. Furthermore, the same samples which exhibited a more oriented crystal structure were closest to the stoichiometric ratio of Zn_3N_2. In contrast, the samples ZnN-1, ZnN-2 and ZnN-6 which deviated to very N-poor and N-rich stoichiometries exhibited broader diffraction peaks, indicative of a large number of defects in their crystal structure. Despite the relative errors associated with standardless EDS analysis,

these results suggest that the composition of the grown films varied significantly with the growth conditions and we were able to obtain substantially N-poor and N-rich films with the range of growth parameters available to us.

TABLE II: Compositional data for different Zn_3N_2 samples as estimated by the quantitative analysis of the EDS spectra.

Sample	C (at. %)	N (at. %)	O (at. %)	Zn (at. %)	Zn:N
ZnN-1	5.04	28.83	10.83	55.31	1.92
ZnN-2	5.97	30.38	12.20	51.45	1.69
ZnN-3	4.22	33.97	9.17	52.64	1.55
ZnN-4	6.17	32.84	11.20	49.79	1.52
ZnN-5	3.50	38.04	5.09	53.38	1.40
ZnN-6	3.70	37.73	11.20	48.05	1.27

B. Electrical properties

The dependence of the electrical properties of Zn_3N_2 films on the growth conditions was also investigated by Hall Effect measurements. The resistivity, carrier concentration and carrier mobility derived from the van der Pauw Hall Effect measurements are shown as a function of growth conditions in **Fig. 4.** The results are listed in detail in **Table III**. The resistivity and carrier mobility of the films grown at 45 SCCM N_2 increased significantly, while the carrier concentration decreased, as shown in **Fig. 4a,b**. As a function of substrate temperature, shown in **Fig. 4c,d**, the resistivity and carrier mobility of the films consistently decreased and increased respectively, while

the carrier concentration overall increased after reaching a minimum for the sample grown at 50 °C.

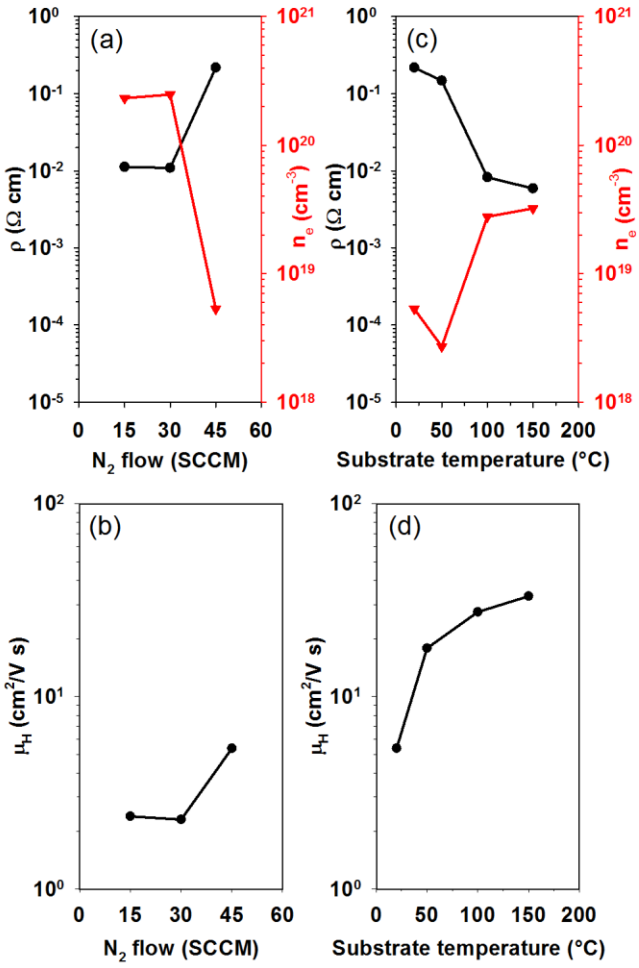

FIG. 4: Resistivity ρ (circles), charge carrier concentration n_e (triangles) and mobility μ_H of grown Zn_3N_2 samples as a function of (a, b) N_2 flow and (c, d) substrate temperature.

A plot of the carrier concentration against the average Zn:N atomic ratio, shown in **Fig. 5a**, shows that the carrier concentration reached a minimum in the samples which were closest to the stoichiometric ratio of Zn_3N_2. This suggests that there was a reduction in the number of native defects which generate charge carriers. N vacancies are considered to cause n-type conductivity in N-poor conditions, while it has been suggested that Zn vacancies and N interstitials will result in p-type conductivity in N-rich conditions[32]. Therefore, we suggest that the reason for the decrease

in carrier concentration in our N-poor films is a decrease in the number of N vacancies, which are less likely to form in increasingly N-rich conditions. Furthermore, the subsequent increase in the carrier concentration of our N-rich films may be related to increased Zn vacancies and N interstitials, which are more likely to form under these conditions. P-type conductivity was not observed in these samples, however, this may be due to the unintentional oxygen doping in the films, as well as a minimum number of N vacancies formed due to the polycrystalline structure of the films, which contribute to the observed n-type character.

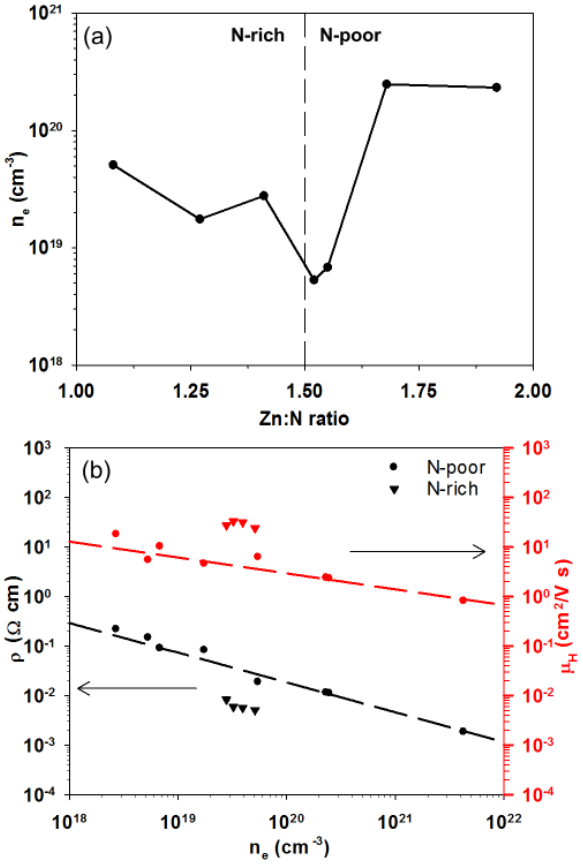

FIG. 5: (a) Carrier concentration (n_e) as a function of the composition of the Zn_3N_2 films. (b) Resistivity (ρ) and charge carrier mobility (μ_H) as a function of carrier concentration Zn_3N_2 samples grown at different conditions. The dashed lines are used as a guide to the eye.

To further investigate the differences in the electrical properties of these samples, the resistivity and carrier mobility of different samples were plotted as a function of the carrier concentration in **Fig. 5b**. Two different profiles were observed in the carrier concentration dependence of resistivity and carrier mobility. In the N-poor samples the resistivity and carrier mobility followed a profile indicative of a natively doped semiconductor, by which they exhibited higher resistivity and carrier mobility at lower carrier concentrations. However, a different profile was observed in the N-rich samples. Specifically, the resistivity was lower and the carrier mobility was higher than in N-poor samples with similar carrier concentrations. This can be explained by the reduced grain boundaries observed in the grain structure of the films grown at these conditions (**Fig. 1e, f**), which should reduce grain boundary scattering and improve the carrier mobility. As the maximum mobility of ~33 $cm^2\ V^{-1}\ s^{-1}$ was achieved in N-rich films with a relatively high charge carrier concentration, further optimization of the growth conditions and film composition could result in even higher charge carrier mobility, as reported in other studies.

TABLE III: Resistivity (ρ), carrier concentration (n_e) and carrier mobility (μ_H) of different Zn_3N_2 samples.

Sample	**Conductivity Type**	**ρ (Ω cm)**	**n_e (cm^{-3})**	**μ_H ($cm^2\ V^{-1}\ s^{-1}$)**
ZnN-1	n-type	1.13×10^{-2}	2.32×10^{20}	2.39
ZnN-2	n-type	1.10×10^{-2}	2.48×10^{20}	2.30
ZnN-3	n-type	2.18×10^{-1}	5.32×10^{18}	5.38
ZnN-4	n-type	1.47×10^{-1}	2.70×10^{18}	17.80
ZnN-5	n-type	8.28×10^{-3}	2.78×10^{19}	27.43

ZnN-6	n-type	5.91×10^{-3}	3.23×10^{19}	33.18

C. Optical properties

With a good understanding of the morphology, composition and crystallinity of the samples, we next investigated their related optical properties. The optical transmittance and reflectance spectra of different Zn_3N_2 samples as well as a fully oxidized sample are shown in **Fig. 6**. Sample ZnN-1 was highly absorbing across the measured spectrum whereas samples grown at higher N_2 flow rates were more transparent in the infrared region, revealing an absorption edge around 1000 nm. The significant amount of excess Zn in samples ZnN-1 and ZnN-2 combined with their poor morphology, evidenced by SEM/EDS, are believed to be the cause of their poor transparency throughout the measured spectrum. The observation of interference fringes in samples ZnN-3 to ZnN-6 shows there was an improvement in the microstructure and thickness uniformity of the films, which reduced the impact of optical scattering, and is therefore in good agreement with the results from SEM. The transmittance spectrum of the oxidized ZnN-3A sample shows the absorption edge shifted to the UV region around 400 nm. The inset image of **Fig. 6** shows the drastic difference in appearance of the as grown and oxidized material as it became transparent in the visible spectrum.

In order to investigate the optical band gap of these films, their absorption coefficient was calculated from these optical measurements. The absorption coefficient calculated for ZnN-3 is shown in **Fig. 7**. The high absorption coefficient ($\alpha > 10^4$ cm^{-1}) obtained in region A shortly after the onset of absorption suggests the dominant transition type is direct, as has been suggested in previous studies[6,10,11,45]. In order to estimate the optical band gap, the expression $(a/hv)^{1/r}$ was plotted against the photon energy, hv. The optical band gap was then estimated at the intersection

of the extrapolated linear region with the energy axis of the diagram. This methodology is based on a property of the absorption coefficient which is derived from the Cody expression for the imaginary part of the dielectric function[46], and is commonly expressed in the following form:

$$\frac{a}{hv} \propto \left(hv - E_g\right)^r \quad (3)$$

where E_g is the optical band gap and r is a constant which describes the type of the dominant transition. Using the value of r = ½ for a direct band gap, it was found that the plots based on the Cody expression had a more distinct linear region and were easier to interpret than those based on the Tauc expression, $(ahv)^{1/r}$, which is more commonly used. This is caused by the increasingly high absorption which is evident in these samples for energies higher than the band gap and is shown in region B of **Fig. 7**. The Cody expression is known to describe semiconductors with high absorption above the band gap more accurately[47], which explains why it is better suited in this case. As a result, we suggest that use of the Tauc expression could lead to an overestimation of the optical band gap of these samples. This is demonstrated in the inset of **Fig. 7** which shows a comparison of the plots obtained by using the two different expressions for sample ZnN-3. Because a reasonable linear fit ($R^2 > 0.99$) could be obtained at a region extended above the band gap, the estimated band gap ranges from 1.4 to 2.2 eV.

An estimate of the optical band gaps and refractive indices of all samples is shown in **Fig. 8a** and **Fig. 8b** respectively. The as grown Zn_3N_2 samples ZnN-3, ZnN-4, ZnN-5 and ZnN-6 have an optical band gap of 1.35, 1.31, 1.32 and 1.48 eV respectively and their refractive index is in the range of 2.3-2.7. In the wide range of Zn_3N_2 films examined here, from N-poor to N-rich, no significant variation of their band gap or refractive index was observed. If the observed optical band gap was caused by N interstitial defects, as has been previously suggested, we would expect a significant blue-shift for the films grown under N-poor conditions, where the formation energy

of N interstitials is larger than other defects[32]. Due to the consistency of the optical properties amongst different samples, we suggest that the optical band gap observed in this material is not defect induced but is instead an intrinsic property of its electronic structure. These optical properties make Zn_3N_2 a candidate for the fabrication of thin film solar cells, which have requirements of high absorption coefficient and a narrow band gap to optimize absorption in the visible spectrum[12].

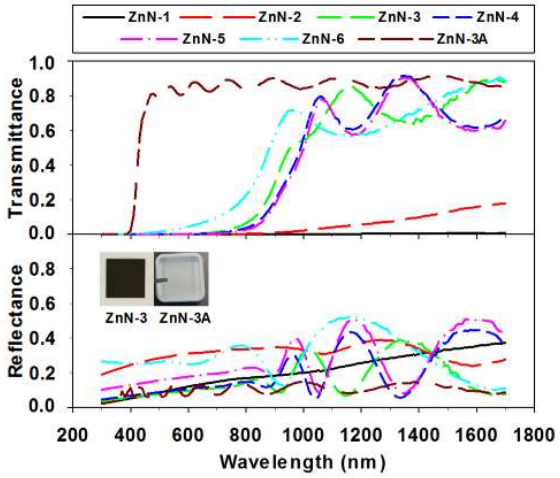

FIG. 6: Optical transmittance and reflectance spectra of samples grown at different N_2 flow rates and substrate temperatures. The inset shows photographs of samples ZnN-3 and ZnN-3A.

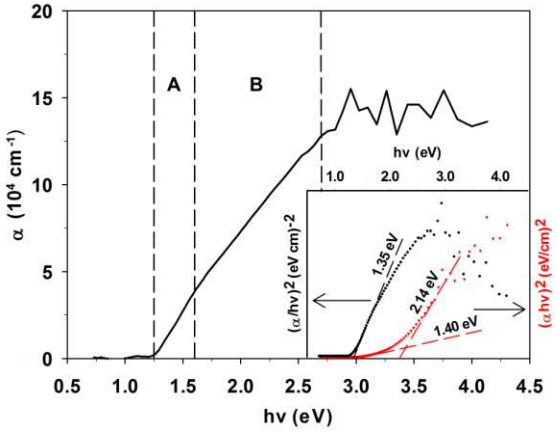

FIG. 7: Absorption coefficient calculated for the sample ZnN-3. Inset: Comparison of the Cody (left) and Tauc (right) expressions for the estimation of the optical band gap of ZnN-3.

A blue shift in the optical band gap, called the Burstein-Moss shift, is often expected in semiconductors with very high carrier concentrations. This has been reported in previous studies[6,11,33] for Zn_3N_2 films with carrier concentrations in the order of 10^{19}-10^{20} cm^{-3}. However, the optical band gap of our samples shows no significant dependence on the carrier concentration. We speculate that some of our samples are in the range of carrier concentrations where the Burstein-Moss effect is becoming apparent. For instance, the blue shift observed in the optical band gap of ZnN-6 could be due to the Burstein-Moss effect, however, there is not enough data to constitute a trend.

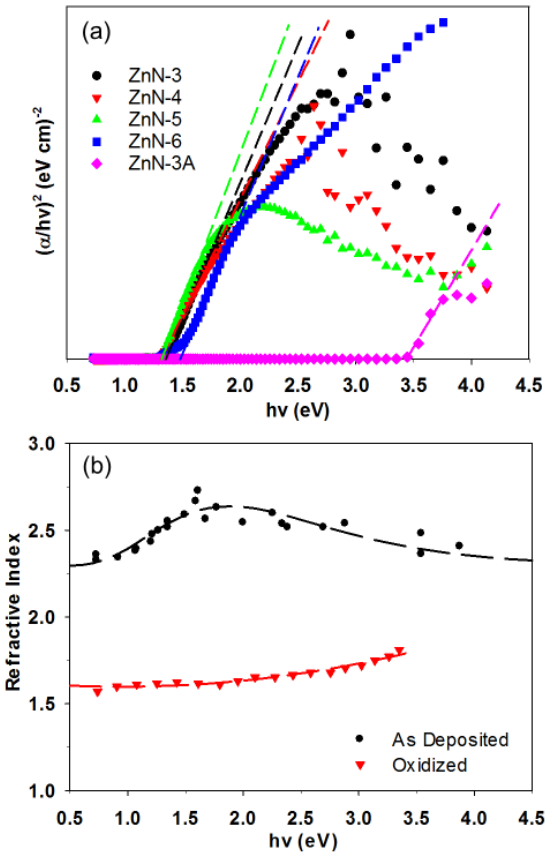

FIG. 8: (a) Absorption plots used to estimate the optical band gap of samples ZnN-3, ZnN-4, ZnN-5, ZnN-6 and ZnN-3A. (b) The refractive index of as deposited and oxidized Zn_3N_2 films as estimated from optical interference fringes in the reflectance spectra.

In contrast to the as grown Zn_3N_2 samples, the optical band gap of the oxidized ZnN-3A sample was estimated at 3.44 eV and its refractive index was in the range of 1.6-1.8. This significant blue-shift of the band gap in ZnN-3A is further clear evidence that it is a different material and matches the conclusion from XRD. The refractive index of the oxidized ZnN-3A sample is closer to the refractive index of $Zn(OH)_2$ minerals[48] which is approximately 1.63, than to pure ZnO, which has a refractive index of 1.9-2.1 in this spectral region[49]. This suggests that the oxidized material does not consist of a pure ZnO phase but is possibly a mixed $ZnO/Zn(OH)_2$ phase. The formation of $Zn(OH)_2$ has been previously reported for Zn_3N_2 films grown with a different technique, and is the result of a reaction of Zn_3N_2 with water[24]. Despite the fact that the XRD pattern of ZnN-3A did not show a $Zn(OH)_2$ phase, the broad ZnO peaks that were observed suggest a large number of structural defects and possibly deviation from stoichiometry.

TABLE IV: Refractive index and optical band gap of Zn_3N_2 films reported here and in previous studies.

Material	**Refractive Index**	**Optical Band Gap (eV)**	**Reference**
Zn_3N_2	2.3-2.7	1.31-1.48	this study
Zn_3N_2	2.0-2.8	< 1.50	Núñez, Pau et al.[18]
Zn_3N_2	2.6-2.8	1.26	Jiang, Georgiev et al.[35]
$ZnO/Zn(OH)_2$	1.6-1.8	3.44	this study
Zn_3N_2	1.8-1.9	3.20-3.50	Simi, Navas et al.[27]
Zn_3N_2	1.7-2.4	3.20	Ayouchi, Casteleiro et al.[34]

A comparison of the optical properties obtained here with these reported in previous publications for Zn_3N_2 is made in **Table IV**. Our results are similar to the results of Núñez, Pau et al. and Jiang, Georgiev et al.[18,35]. However, the properties reported by Ayouchi, Casteleiro et al. and Simi, Navas et al.[27,34] are more similar to the optical properties of our oxidized ZnN-3A sample. The similarity between the optical properties of $ZnO/Zn(OH)_2$ and the properties reported for Zn_3N_2 in these publications seems to support the argument that the wider band gap reported in literature is the result of unintentional oxidation rather than a difference in material quality.

IV. CONCLUSION

Zn_3N_2 thin films were deposited on borosilicate glass slides by DC magnetron sputtering of a Zn target in N_2 plasma. A variety of different growth conditions were employed by varying the N_2 flow in the chamber as well as the substrate temperature during growth, which resulted in the growth of Zn_3N_2 films with different microstructures and degrees of crystallinity as well as a wide range of compositions. XRD measurements of an oxidized sample revealed that the as grown Zn_3N_2 films were converted to a polycrystalline ZnO-based structure after prolonged ambient exposure. Hall Effect measurements showed that the properties of the N-poor Zn_3N_2 samples were indicative of a natively doped semiconductor. As the N-poor films became more stoichiometric, the carrier concentration reached a minimum in the order of 10^{18} cm^{-3}, followed by an increase in resistivity and mobility. N-rich films reached a maximum carrier mobility of 33 cm^2 V^{-1} s^{-1} despite a higher carrier concentration. This is believed to be due to an improvement in the microstructure of the films grown at these conditions. These results show that precise control of the composition of the Zn_3N_2 films grown by reactive sputtering is very important for the optimization of their electrical properties and the subsequent development of applications.

Optical measurements showed that the films formed an absorption edge in the wavelength region of 1000 nm as the film composition approached the stoichiometry of Zn_3N_2. The optical band gap and refractive index of these samples were estimated in the range of 1.31-1.48 eV and 2.3-2.7 respectively, while the optical band gap and refractive index of the oxidized sample were 3.44 eV and 1.6-1.8 respectively. The Zn_3N_2 films had high absorption coefficient indicative of a direct band gap semiconductor as well as high absorption for energies higher than the band gap, which we suggest could lead to an overestimation of the optical band gap. Neither the refractive index nor the optical band gap of the Zn_3N_2 films varied significantly despite the wide range of samples examined. This suggests that the observed optical band gap is an intrinsic property of this material and is not defect induced, which makes Zn_3N_2 a candidate for applications in thin film solar cells.

ACKNOWLEDGEMENTS

This project was co-funded by the EPSRC (Engineering and Physical Science Research Council) and Johnson Matthey PLC (Award No. 14550005). The financial support by these parties is highly appreciated.

REFERENCES

[1] E. Aperathitis, V. Kambilafka, and M. Modreanu, Thin Solid Films **518,** 1036 (2009).

[2] C. G. Núñez, J. L. Pau, E. Ruiz, and J. Piqueras, Applied Physics Letters **101,** 253501 (2012).

[3] S. R. Bhattacharyya, R. Ayouchi, M. Pinnisch, and R. Schwarz, physica status solidi (c) **9,** 469 (2012).

[4] K.-C. Ok, H.-J. Jeong, H.-M. Lee, J. Park, and J.-S. Park, Ceramics International **41,** 13281 (2015).

[5] S. Sinha, D. Choudhury, G. Rajaraman, and S. K. Sarkar, RSC Advances **5,** 22712 (2015).

[6] M. Futsuhara, K. Yoshioka, and O. Takai, Thin Solid Films **322,** 274 (1998).

[7] F. Zong, H. Ma, W. Du, J. Ma, X. Zhang, H. Xiao, F. Ji, and C. Xue, Applied Surface Science **252,** 7983 (2006).

[8] V. Kambilafka, P. Voulgaropoulou, S. Dounis, E. Iliopoulos, M. Androulidaki, K. Tsagaraki, V. Šály, M. Ružinský, P. Prokein, and E. Aperathitis, Thin Solid Films **515,** 8573 (2007).

[9] V. Kambilafka, A. Kostopoulos, M. Androulidaki, K. Tsagaraki, M. Modreanu, and E. Aperathitis, Thin Solid Films **520,** 1202 (2011).

[10] C. G. Núñez, J. L. Pau, M. J. Hernández, M. Cervera, E. Ruiz, and J. Piqueras, Thin Solid Films **520,** 1924 (2012).

[11] T. Suda and K. Kakishita, Journal of Applied Physics **99,** 076101 (2006).

[12] M. A. Green, Journal of Materials Science: Materials in Electronics **18,** 15 (2007).

[13] K. Kuriyama, Y. Takahashi, and F. Sunohara, Physical Review B **48,** 2781 (1993).

[14] F. J. Zong, H. L. Ma, C. S. Xue, H. Z. Zhuang, X. J. Zhang, H. D. Xiao, J. Ma, and F. Ji, Solid State Communications **132,** 521 (2004).

[15] G. Paniconi, Z. Stoeva, R. I. Smith, P. C. Dippo, B. L. Gallagher, and D. H. Gregory, Journal of Solid State Chemistry **181,** 158 (2008).

[16] W. S. Khan and C. Cao, Journal of Crystal Growth **312,** 1838 (2010).

[17] G. Z. Xing, D. D. Wang, B. Yao, L. F. N. A. Qune, T. Yang, Q. He, J. H. Yang, and L. L. Yang, Journal of Applied Physics **108,** 083710 (2010).

[18] C. G. Núñez, J. L. Pau, M. J. Hernández, M. Cervera, and J. Piqueras, Applied Physics Letters **99,** 232112 (2011).

[19] A. H. Jayatissa and T. Wen, Surface and Coatings Technology **211,** 163 (2012).

[20] J. M. Khoshman, N. Peica, C. Thomsen, J. Maultzsch, B. Bastek, C. Wan, and M. E. Kordesch, Thin Solid Films **520,** 7230 (2012).

[21] N. Jiang, D. G. Georgiev, T. Wen, and A. H. Jayatissa, Thin Solid Films **520,** 1698 (2012).

[22] T. Wen, M. Gautam, A. M. Soleimanpour, and A. H. Jayatissa, Materials Science in Semiconductor Processing **16,** 318 (2013).

[23] P. N. Taylor, M. A. Schreuder, T. M. Smeeton, A. J. D. Grundy, J. A. R. Dimmock, S. E. Hooper, J. Heffernan, and M. Kauer, Journal of Materials Chemistry C **2,** 4379 (2014).

[24] K. Toyoura, H. Tsujimura, T. Goto, K. Hachiya, R. Hagiwara, and Y. Ito, Thin Solid Films **492,** 88 (2005).

[25] S. Sinha and S. K. Sarkar, RSC Advances **4,** 47177 (2014).

[26] J. M. Erie, Y. Li, M. Ivill, H. S. Kim, S. J. Pearton, B. Gila, D. P. Norton, and F. Ren, Applied Surface Science **254,** 5941 (2008).

[27] S. Simi, I. Navas, R. Vinodkumar, S. R. Chalana, M. Gangrade, V. Ganesan, and V. P. M. Pillai, Applied Surface Science **257,** 9269 (2011).

[28] D. Wang, Y. C. Liu, R. Mu, J. Y. Zhang, Y. M. Lu, D. Z. Shen, and X. W. Fan, Journal of Physics: Condensed Matter **16,** 4635 (2004).

[29] E. Maile and R. A. Fischer, Chemical Vapor Deposition **11,** 409 (2005).

[30] P.-C. Wei, S.-C. Tong, C.-M. Tseng, C.-C. Chang, C.-H. Hsu, and J.-L. Shen, Journal of Applied Physics **116** (2014).

[31] T. Oshima and S. Fujita, Japanese Journal of Applied Physics **45,** 8653 (2006).

[32] N. Jiang, J. L. Roehl, S. V. Khare, D. G. Georgiev, and A. H. Jayatissa, Thin Solid Films **564,** 331 (2014).

[33] X. Cao, A. Sato, Y. Ninomiya, and N. Yamada, The Journal of Physical Chemistry C **119,** 5327 (2015).

[34] R. Ayouchi, C. Casteleiro, L. Santos, and R. Schwarz, physica status solidi (c) **7,** 2294 (2010).

[35] N. Jiang, D. G. Georgiev, A. H. Jayatissa, R. W. Collins, J. Chen, and E. McCullen, Journal of Physics D: Applied Physics **45,** 135101 (2012).

[36] C. G. Núñez, J. L. Pau, M. J. Hernández, M. Cervera, E. Ruíz, and J. Piqueras, Thin Solid Films **522,** 208 (2012).

[37] D. Ritter and K. Weiser, Optics Communications **57,** 336 (1986).

[38] J. A. Bearden, Reviews of Modern Physics **39,** 78 (1967).

[39] M. O. Krause and J. H. Oliver, Journal of Physical and Chemical Reference Data **8,** 329 (1979).

[40] N. W. Ritchie, Scanning **35,** 141 (2013).

[41] D. E. Partin, D. J. Williams, and M. O'Keeffe, Journal of Solid State Chemistry **132,** 56 (1997).

[42] E. R. Jette and F. Foote, The Journal of Chemical Physics **3,** 605 (1935).

[43] S.-H. Yoo, A. Walsh, D. O. Scanlon, and A. Soon, RSC Advances **4,** 3306 (2014).

[44] Y.-N. Xu and W. Y. Ching, Physical Review B **48,** 4335 (1993).

[45] A. H. Jayatissa, T. Wen, and M. Gautam, Journal of Physics D: Applied Physics **45,** 045402 (2012).

[46] G. Cody, *Hydrogenated amorphous silicon, Part B, Optical properties, semiconductors and semimetals* (Orlando: Academic Press Vol, 1984).

[47] A. C. Diebold, in *Advances in Solid State Physics* (Springer, 2009), p. 371.

[48] J. W. Anthony, R. A. Bideaux, K. W. Bladh, and M. C. Nichols, (Mineralogical Society of America, Chantilly, USA).

[49] W. L. Bond, Journal of Applied Physics **36,** 1674 (1965).